Magnetization transfer magic-angle-spinning z-spectroscopy of excised tissues

Reut Avni [a], Oren Mangoubi [a], Rangeet Bhattacharyya [a], Hadassa Degani [b], Lucio Frydman [a,*]

[a] Departments of Chemical Physics, Weizmann Institute of Science, 76100 Rehovot, Israel
[b] Departments of Biological Regulation, Weizmann Institute of Science, 76100 Rehovot, Israel

ABSTRACT

NMR experiments devised to aid in analyses of tissues include magnetization transfer (MT), which can highlight the signals of biological macromolecules through cross-relaxation and/or chemical exchange processes with the bulk ^{1}H water resonance, and high-resolution magic-angle-spinning (HRMAS) methods, akin to those used in solid-state NMR to introduce additional spectral resolution via the averaging of spin anisotropies. This paper explores the result of combining these methodologies, and reports on MT "z-spectroscopy" between water and cell components in excised tissues under a variety of HRMAS conditions. Main features arising from the resulting [1]H "MTMAS" experiments include strong spinning sideband manifolds centered at the liquid water shift, high-resolution isotropic features coinciding with aliphatic and amide proton resonances, and a second sideband manifold arising as spinning speeds are increased. Interpretations are given for the origin of these various features, including simulations shedding further light onto the nature of MT NMR signals observed for tissue samples. Concurrently, histological examinations are reported validating the limits of HRMAS NMR procedures to the analysis of tissue samples preserved in a number of different ways.

© 2009 Elsevier Inc. All rights reserved.

1. Introduction

Nuclear Magnetic Resonance (NMR) is a valuable tool for the analysis and characterization of biological samples. Spectra of tissues and cell extracts can provide important biochemical information, and spectroscopic observations have contributed substantially to a better understanding of the metabolic profiles in both ex- and in-vivo systems [1–7]. The usefulness of the basic 1D NMR measurement has also been enhanced in a number of ways over the years; among the techniques used in the analysis of biological tissues are the magnetization transfer (MT) protocol for enhancing the sensitivity and contrast of macromolecular structures, and the high-resolution magic-angle-spinning (HRMAS) NMR experiment for the sake of improving spectral resolution. The present work examines the features arising upon merging these two methods into a combined tool: the ^{1}H MTMAS NMR experiment.

MT is a physical phenomenon first exploited within a small-molecule NMR setting by Forsen and Hoffman [8], and which has been widely used in biomedical studies to enhance the spectral response of minority constituents in tissues and organs [9–15]. MT NMR relies on the heterogeneous mixture that makes up biological tissues, involving an easily detectable H_2O liquid signal, and a low-sensitivity background including metabolites and the tissue ma-

trix. From an NMR perspective tissues can be considered composed of intimately mixed but spectroscopically-speaking very different spin sub-ensembles, which can exchange their magnetizations by a variety of routes. "z-spectroscopy" MT exploits this net transfer to characterize the lower-abundance, short-T_2 species, by monitoring their effect on the high population of mobile, long-T_2 protons in the liquid water. The precise mechanism(s) of the transfer are still a topic of research; they can involve cross-relaxation or spin diffusion effects [10–16], as well as a chemical exchange pathway whereby the labile protons of certain side groups (–OH, –SH, –NH) interchange with the water population leading to Chemical Exchange Saturation Transfer (CEST) [17–21]. Recent years have witnessed many biological NMR applications of both the MT and the CEST experiments. Starting from Wolff and Balaban's demonstration of MT as a mean for producing in-vivo imaging contrast [9], there has been a growing use of this phenomenon in clinical diagnosis of conditions such as Alzheimer disease and other brain atrophies [22–24], multiple sclerosis [25], breast cancer [26], and cartilage degeneration [27,28]. CEST has also seen a growing number of applications including the in-vivo detection of metabolites [29,30], imaging of proteins [31], pH monitoring [32], measurements of enzyme-catalyzed reactions [33,34], and the development of "smart" contrast imaging agents having several exchangeable sites [35–37]. Regardless of whether operating through MT or CEST mechanisms, exchange with the water spin reservoir is exploited by all these studies to facilitate the detection of signals arising from minority components of a tissue. In, all these

cases saturating these components will, owing to an exchange process of rate k^{MT} with the solvent, result in a decrease of the sharp and easily observable H_2O signal. This results in a magnification of the low-abundant ^1H reservoir by factors on the order of $k^{MT} \cdot T_1^{H_2O}$, which for optimal cases can reach up to 10^3–10^4.

High-resolution NMR spectra of biological tissues are usually difficult to obtain due to interferences stemming from the anisotropic character of the spin interactions, which may lead to broad lines. This is especially true for crystalline solids but also for the more rigid parts of tissues, such as membranes, proteins, phospholipids, or in general any motionally-restricted, large macromolecules. Broad line shapes $I(\omega)$ will then originate even from single chemical sites due to the (θ, ϕ) orientational dependence that spin interactions possess vis-à-vis Bo [38]:

$$I[\omega_{aniso}(\theta, \varphi)] = I\left[\delta_{aniso}\left(\frac{3\cos^2\theta - 1}{2} + \eta_{aniso}\sin^2\theta\cos 2\varphi\right)\right] \quad (1)$$

where δ_{aniso} and η_{aniso} are intrinsic parameters defining the strength and asymmetry of the anisotropies. For nearly five decades [39,40], MAS NMR has offered a way of reducing the influence of these second-rank line broadening factors. This technique involves mechanically spinning the sample at a rate ω_r, while subtending an angle $\beta = 54.74°$ with respect to the external field B_0. Upon doing so a time-dependence on the susceptibility, the chemical shift and the dipolar spin anisotropies is imposed [41]:

$$\omega_{aniso}(\theta', \varphi', \phi'; t) = \left(\frac{3\cos^2\beta - 1}{2}\right)\left[\delta_{aniso}\left(\frac{3\cos^2\theta' - 1}{2}\right.\right.$$
$$\left.\left. + \eta_{aniso}\sin^2\theta'\cos 2\varphi'\right)\right] + g_1(\beta, \theta', \varphi')\cos(\omega_r t + \phi')$$
$$+ g_2(\beta, \theta', \varphi')\cos(2\omega_r t + 2\phi') \quad (2)$$

where the $\{g_i\}_{i=1,2}$ are time-independent functions and the $(\theta', \phi', \varphi')$ set refers now to Euler orientations with respect to a reference frame fixed on the rotor. If spinning the sample occurs sufficiently fast one can consider solely the average value of these frequencies, leading to sharp lines for every inequivalent site. HRMAS on tissues [42,43] has proved advantageous in studies of biopsied specimens from brain [44], breast [45] and kidney [46], helping to differentiate between malignant and benign cells based on differences in their metabolite profiles.

In view of the features just summarized, we considered it worth examining the potential effects arising upon combining the sensitivity enhancing properties of MT NMR, with the high-resolution properties of HRMAS. By doing so we hoped to help clarify the groups contributing to the main features of MT under ex (and eventually under in) vivo conditions. These efforts are akin to those recently reported by Singer and coworkers [47], except for our focus on the strong H_2O peak rather than on the signals arising from the metabolic components. The following sections summarize the methodology adopted toward this end, and the main results that were observed with the resulting "MTMAS" approach.

2. Materials and methods

2.1. Proton NMR spectroscopy

Most NMR experiments in this study were performed on a Varian InfinityPlus® 600 MHz NMR spectrometer using a 4 mm double-resonance probe. For every spinning speed assayed, two complementary data sets were recorded: a conventional single-pulse ^1H HRMAS NMR spectrum to assess tissue viability (100 transients, 50 kHz spectral width, 163 ms acquisition time), and an MT experiment collected under MAS conditions. These latter experi-
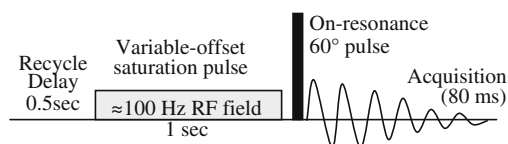

Fig. 1. Typical experimental parameters used in the MTMAS NMR acquisitions.

ments were performed using the pulse scheme illustrated in Fig. 1, involving an initial saturating RF irradiation whose offset was sequentially stepped between +25 and −25 kHz from the water resonance, followed by an optimized water-monitoring pulse. The γB_1^{sat} RF saturation field was set to ~100 Hz, and two phase-cycled repetitions were collected for each saturation offset. As the saturating RF was swept using 50 Hz offset increments a total of 1001 1D data sets were collected per MTMAS acquisition; these data were plotted in a standard "z-spectrum" format [35], showing the relative attenuation of the water z-magnetization as a function of the saturating RF offset. In order to clarify certain spectral features complementary MTMAS experiments were also performed on a 300 MHz spectrometer, equipped with a Bruker 4 mm double-resonance probe and controlled by an Apollo® Tecmag console.

2.2. Preparation of phantom samples

Three semi-solid model systems were chosen to evaluate the origin of the different peaks observed in MTMAS experiments on excised tissues. These included 10% Gelatin as an example of protein matrix, a 6% Agar gel as polysaccharide model, and 3:2 DHPC-DMPC suspensions of bicelles (Avanti Polar Lipids) forming a gel phase at 4 °C as model for membranes.

2.3. Tissue specimens

All procedures were carried out following our Institute's Animal Care and Use Committee approval. Different mice tissue samples including brain, liver, spleen, kidney and muscle specimens were targeted in the studies. Given the potential mechanical stresses involved in the HRMAS procedure, a number of protocols were assayed in the examination of these samples. Some specimens were subject to slow cooling by placement in aluminum paper and storage in a vial with dry ice, while others underwent rapid freezing by insertion into a liquid nitrogen vial immediately following their excision. After performing both types of freezing procedures, the specimens were kept refrigerated at −80 °C until investigated by NMR (1–3 months). A third set of tissue samples was taken and analyzed immediately after excision without any freezing and/or storing procedures, within a maximum of 6 h after sacrifice. Approximately 50 mg were used for each MTMAS test; these specimens were sliced to fit a 4 mm outer diameter MAS rotor (~50 μl volume with top and bottom spacers), and transferred to a pre-cooled NMR probe for observations at 4 °C. In order to check the integrity of the examined tissues upon performing the NMR experiments, different muscle specimens were also taken for subsequent histological examinations.

2.4. Histological examinations

To estimate how the freezing, storage and spinning of the samples at different rates for relatively long periods of time would affect the integrity of the tissues, multiple muscle specimens were taken for histological examination. These were conducted both at the end of the three modes of preparation described above (slow
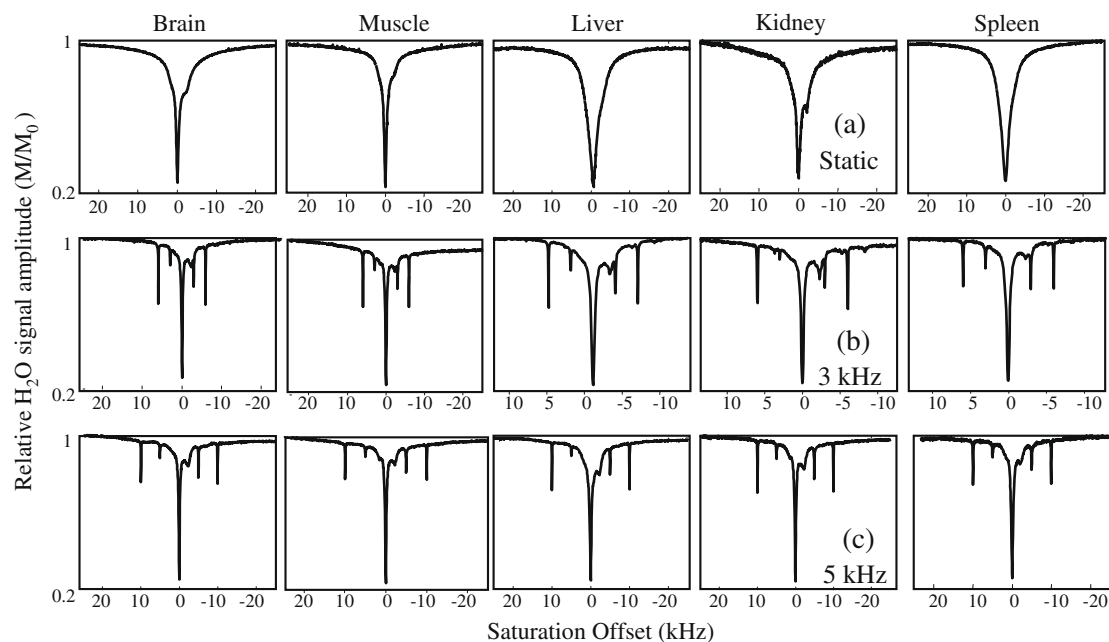
Fig. 2. MT z-spectra recorded for the indicated tissues under (a) static, (b) 3 kHz, and (c) 5 kHz MAS conditions. For most of the experiments, the RF was swept from −25 kHz to +25 kHz using 50 Hz offset increments. For liver, kidney and spleen at 3 kHz MAS, the RF was swept from −11 kHz to +11 kHz. M and M_0 denote the signals arising from the water magnetization under steady state saturation and equilibrium conditions, respectively. All spectra were obtained at 600 MHz and 4 °C using the sequence in Fig. 1.

dry-ice freeze, sudden l-N$_2$ freeze, fresh), as well as at the conclusion of the corresponding HRMAS experiments. For these various samples three spinning speeds and one control set were validated, including very high (14 kHz and above), high (10 kHz), low (3–4 kHz) and zero spinning rates. The tissues involved in these histological analyses were fixed in formaldehyde and embedded in Paraffin blocks; 4 μm sections were then stained with hematoxylin-eosin (H&E) under standard conditions [48] and assessed by light microscopy examination.

3. Results

3.1. General features of ^{1}H MTMAS NMR

Fig. 2 displays representative MTMAS NMR z-spectra for different tissues measured at 4 °C, at 0, 3 and 5 kHz spinning speeds. All MTMAS NMR traces display certain features in common, and these features were qualitatively preserved for all sample preparation protocols including samples which were measured 'fresh' without any handling or storage, and samples that underwent freezing with dry ice or liquid nitrogen and storage at −80 °C until their NMR examination. Beyond the basic on-resonance saturation at zero frequency, all MTMAS experiments display a number of new absorptions that are absent in the static case. These features include a sideband manifold with very sharp (≈50–100 Hz) absorptions whose center of mass falls at the exact isotropic frequency of H$_2$O, and a small number of narrow lines that flank the H$_2$O centerband. The sidebands are the most dominant new feature arising upon executing MAS, and are reminiscent of the pattern that one would expect to arise from the time-dependent $\{g_i\}_{i=1.2}$ functions in Eq. (2) upon averaging out semi-solid spin anisotropies. Then again, looking closely at these MAS sideband patterns, a number of features appear quite unusual. For instance:

- Despite the different nature of the analyzed tissues, nearly identical MTMAS sideband patterns emerge for all specimens.

- These sidebands do not fit the typical intensities expected upon spinning solid-like NMR anisotropies, since regardless of the spinning rate assayed they exhibit strong first and second sidebands but nearly no third of fourth order ones.
- The sidebands' intensities depend only weakly on spinning speed, and do not exhibit the typical ω_r dependencies predicted by a Herzfeld–Berger analysis of solid-state NMR anisotropies [41].

All this suggests that these MTMAS saturation sidebands do not stem from semi-solid "structural" H$_2$Os, but rather are an intrinsic feature associated with this kind of experiments. Final confirmation for this suspicion is given by Fig. 3, which shows that MTMAS spectra of liquid water at different spinning speeds produce similar kinds of sideband patterns as semi-solid tissues. Off-MAS MT traces recorded while spinning perpendicular to the external B_0 (not shown) were also characterized by relatively sharp spinning sidebands manifolds, appearing at $\pm\omega_r$ and $\pm2\omega_r$ rather than at the sole even multiples of ω_r as predicted by Eq. (2).

3.2. The origin of the dominant MTMAS sideband patterns

It follows that the dominant MT sideband manifolds do not arise from typical MAS-derived field modulations of the spin anisotropies. Instead, we attribute these sideband patterns to B_1-related RF inhomogeneities, which upon undergoing MAS acquire a periodic time-modulation capable of back-saturating the liquid water even under off-resonance irradiation conditions. Supporting this model is the fact that the MTMAS H$_2$O sidebands were highly influenced by the NMR probe used for the measurement (cf. Fig. 5, below); no other factor—including B_0 inhomogeneities—showed a similar influence.[1] In order to better understand how B_1 inhomogeneities can generate the observed sidebands, we revisit the effect of

---

[1] In fact, B_0 inhomogeneities could not account for these modulations, since the extent of the macroscopic magnetic susceptibilities ΔB_0, is in the order of 100 Hz. As spinning speeds much larger than these ΔB_0 were used, one would not expect to observe sidebands under such inhomogeneity conditions.
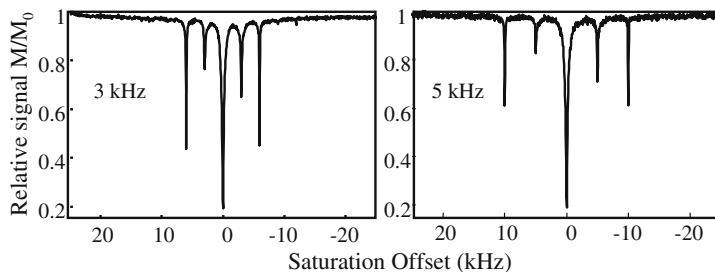
Fig. 3. MTMAS z-spectra recorded under conditions akin to those in Fig. 2, for a liquid water sample at 3 and 5 kHz spinning speeds.

the RF on a spin packet along the course of the MAS rotation. If the solenoid RF coil produces an ideal B_1 field, perfectly parallel to and concentric with the axis of sample rotation, then MAS would impose no time-modulations and no sidebands would arise. But as noted by Hoult and Richards [49] and examined in further detail by Tekely, Engelke and coworkers [50,51], non-idealities in the coil can also generate spatially-dependent B_1 components that will become frequency modulated by $\pm\omega_r$, $\pm 2\omega_r$ offsets upon imposing the MAS. These non-idealities will in general stem from a solenoid that is not infinite and perfectly symmetric along its main Z-axis. This will result in a radial field component B_1^{rad} in addition to the ideal B_1^{ax} axial one; when subject to MAS spins will traverse this radial field flux, and feel a $\cos(\omega_r t + \varphi)$ phase modulation superimposed onto B_1^{rad}. This appears as an RF field that is offset by $\pm\omega_r$ from the basic carrier irradiation. Moreover, if the main axis of sample spinning is not perfectly collinear within the solenoid, an additional amplitude modulation of the axial and radial B_1 components may occur. This brings about a $\cos(\omega_r t + \varphi)$ modulation of the axial field component and a $\cos(2\omega_r t + \varphi)$-type modulation of the radial one, equivalent to having off-resonant offset components at once and twice the spinning rate modulating the basic carrier frequency. All these non-idealities are schematically described in Fig. 4.

A simple way of visualizing how these additional $\pm\omega_r$, $\pm 2\omega_r$ B_1 modulations will generate the sidebands observed in the MTMAS experiment, results from considering the spin irradiation Hamiltonian in a rotating-frame centered at the water chemical shift. Given an RF presaturation field of amplitude γB_1, off-resonance $\delta\omega$ and phase φ at time $t = 0$, this Hamiltonian becomes:

$$
\begin{aligned}
H_{RF}(t) &= \gamma B_{1,X}(t)I_x + \gamma B_{1,Y}(t)I_y \\
&= \gamma B_1[\cos(\delta\omega \cdot t + \varphi) \cdot I_x + \sin(\delta\omega \cdot t + \varphi) \cdot I_y] \\
&= \frac{\gamma B_1}{\sqrt{2}}[I_- e^{+i(\delta\omega \cdot t + \varphi)} - I_+ e^{-i(\delta\omega \cdot t + \varphi)}]
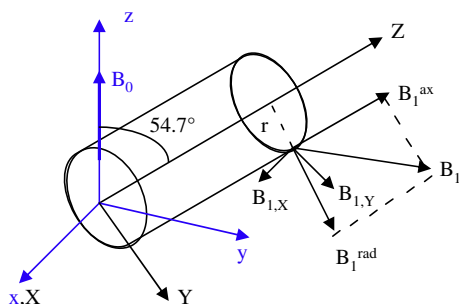\end{aligned}
\tag{3}
$$

Fig. 4. Schematic representation of how the different B_1 components in an (X,Y,Z) coil frame (black), map into an (x,y,z) lab frame (blue). For a distance r away from the coil's center, a spin packet experiences a field with projections B_1^{ax}, B_1^{rad} (the latter shown much larger than in reality); upon computing the spins' evolution, these radial and axial components of B_1 need to be projected into the lab frame, and then the effects of components perpendicular to B_0 transformed into a rotating-frame. (For interpretation of the references to colour in this figure legend, the reader is referred to the web version of this article.)

If now, according to the arguments of the proceeding paragraph, MAS imparts on the amplitude of the irradiation field a time-dependence involving $\pm\omega_r$, $\pm 2\omega_r$ terms:

$$
B_1(\vec{r}, t) = \sum_{n=-2}^{+2} B_1^{(n)}(\vec{r})e^{in\omega_r t}
\tag{4}
$$

(where $\{\vec{r}\}$ denotes the position of the spin within the rotor, a heterogeneity that for the sake of simplicity we shall from here on disregard), it follows that the Hamiltonian will acquire additional time dependencies on top of the constant offset $\delta\omega$. Inserting these into H_{RF}, it becomes clear that a time-independent irradiation that is permanently on-resonance with the water peak at $\delta\omega = 0$, will arise when:

$$
\delta\omega = n\omega_r \quad n = -2, -1, 0, +1, +2
\tag{5}
$$

For these cases the average RF Hamiltonian becomes:

$$
< H_{RF} > = \frac{\gamma}{\sqrt{2}}[B_1^{(-n)}e^{i\varphi}I_- - B_1^{(+n)}e^{-i\varphi}I_+]
\tag{6}
$$

and one ends up with a time-independent, on-resonance RF, which we ascribe as the basis for the saturation sidebands observed in MTMAS experiments. Disregarding the phases in Eq. (6), which are not relevant when considering spin saturation, the effective RF field accomplishing this phenomenon becomes

$$
\gamma B_{eff}^n = \gamma\sqrt{2[(B_1^{(n)})^2 + (B_1^{(-n)})^2]}
\tag{7}
$$

A steady-state solution of the Bloch equations for spins feeling these on-resonance components, will then exhibit an attenuated z-magnetization

$$
\frac{M_z}{M_0} = \frac{1}{1 + T_1 T_2 \{\gamma B_{eff}^{(n)}\}^2}
\tag{8}
$$

Overall it follows that, when irradiating at offsets $\delta\omega = \pm\omega_r$, $\pm 2\omega_r$, the two coil-related sources of non-idealities mentioned earlier can restore "on-resonance" fields that, although arguably weaker than the direct on-resonance irradiation, act very much like the latter regardless of the magnitude of ω_r. This explains why the observed MTMAS sidebands have narrower linewidths than the central saturation band ($\leqslant 100$ Hz versus ≈ 500 Hz), why they exhibit such a weak ω_r-dependence, and why no sidebands are evident for $|n| \geqslant 3$.

Having clarified these features, we turn next to a numerical quantification of what kind of non-idealities would be needed to reproduce the kind of sideband manifolds revealed by the MTMAS. For doing so we follow the model given in Ref. [51], and represent the MAS-imposed time-dependencies of B_1^{rad} and B_1^{ax} by a Fourier series whose coefficients represent different non-idealities within the coil. Given the clearly asymmetric features displayed by the experimental MTMAS traces, at least three $\{a_i\}_{i=1-3}$ coefficients were needed to define the axial and radial field non-idealities arising in the experiments:

$$B_1^{ax} = b_1^{ax}[1 + a_1\cos(\omega_r t) + a_3\cos(2\omega_r t)]$$
$$B_1^{rad} = b_1^{ax} a_2 \tag{9}$$

Here, B_1^{ax} denotes the axial RF field generated by the coil, which should ideally be perfectly coaxial with the MAS axis and uniform throughout the sample. In principle these $\{a_i\}_{i=1-3}$ should be spatially-dependent but, for simplicity, they were assumed constant throughout the sample. To fully account for the effects of these fields, the time-dependencies of the B_1^{ax} and B_1^{rad} components need to be transformed to the rotating frame using the relationships:

$$B_{1,X}(t) = B_1^{rad}\cos(\omega_r t)$$
$$B_{1,Y}(t) = \sqrt{\frac{2}{3}}B_1^{ax} + \sqrt{\frac{1}{3}}B_1^{rad}\sin(\omega_r t) \tag{10}$$

Using then the B_1^{ax} and B_1^{rad} from Eq. (9), the rotating frame $B_{1,X}$, $B_{1,Y}$ components appearing in Eq. (3) can be written as

$$B_{1,X}(t) = b_1^{ax} a_2 [\cos(\omega_r t)]$$
$$B_{1,Y}(t) = \sqrt{\frac{2}{3}}b_1^{ax}[1 + a_1\cos(\omega_r t) + a_3\cos(2\omega_r t)] + \sqrt{\frac{1}{3}}a_2\sin(\omega_r t) \tag{11}$$

With these expressions at hand, the calculations summarized in the Appendix were used to find which $\{a_i\}_{i=1-3}$ parameters could reproduce the experimental MTMAS sidebands. As can be seen from Fig. 5 this model successfully reproduces the MTMAS patterns observed at independent 600 and 300 MHz machines, even if with RF inhomogeneity parameters that differ for these two fields due to the different properties of the probes employed in each case. As predicted, the sideband intensities are nearly independent of spinning speed and show negligible contributions unless $n = \pm1$, ±2.

Still, even these sidebands exhibit a small decrease in their intensities with spinning rate; a possible explanation for this may rest in the spatial dependencies that were neglected for the $\{a_i\}_{i=1-3}$ coefficients. Also worth pointing out is that although the saturating RF field was set to ~100 Hz, the effective fields at the $\pm\omega_r$, $\pm2\omega_r$ frequencies are scaled by $\{a_i\}_{i=1-3}$ coefficients; therefore, the sidebands appear smaller and narrower than the main $n = 0$ H_2O saturation peak. A final point noticing in connection to Fig. 5 concerns the asymmetries evidenced by the sideband patterns. It is known that radiation damping together with probe detuning, especially in high fields, can introduce asymmetry into a z-spectrum [52]. However, MTMAS experiments done when the probe was detuned by +1 MHz and by −1 MHz showed the sidebands' asymmetry virtually unchanged. We, therefore, believe that all asymmetry effects are solely reflecting non-idealities stemming from imperfect geometrical arrangements of the different RF coils and their spinners.

3.3. High-resolution isotropic features of MTMAS spectra

In addition to the dominating sideband patterns just discussed, the MTMAS traces show a spectral resolution enhancement compared to the static case. For most of the analyzed tissues this included the appearance of three features at ≈1.2, 1.8 and 7.3 ppm that could be discerned at even relatively slow spinning rates; an additional shoulder at ~6.8 ppm was revealed in the MTMAS traces of some tissues. In order to identify the chemical origin of these resolved saturation peaks, a series of MTMAS tests were run on model semi-solid samples. As can be seen in Fig. 6, the high-resolution tissue features are also visible in the MTMAS trace of Gelatin (a protein sample), but not in semi-solids made up from Agar (a poly-
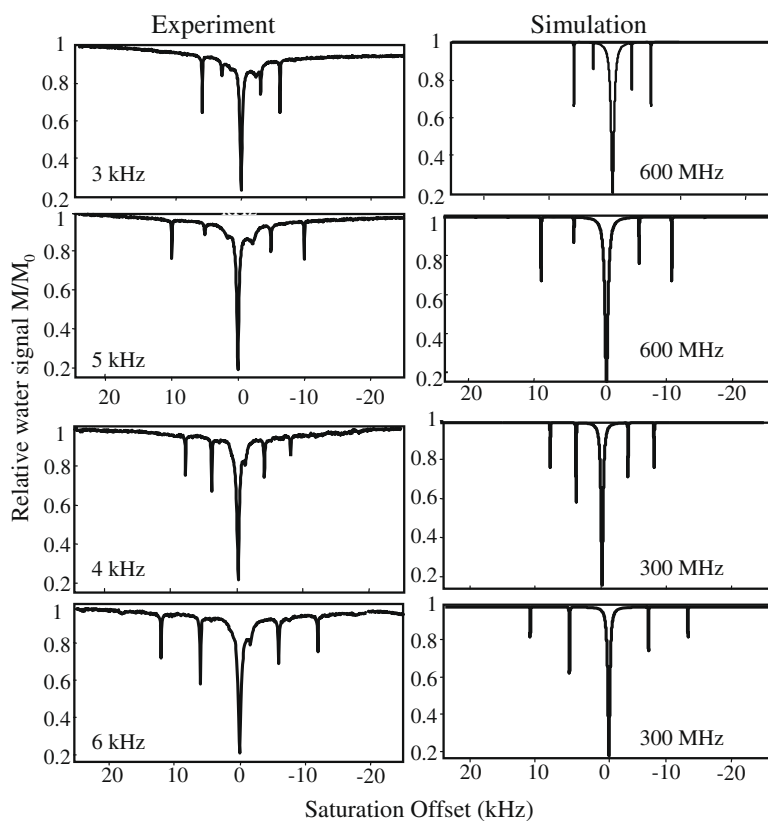

Fig. 5. Comparison between MTMAS lineshapes calculated based on steady state solutions of the Bloch equations (right) and experimental muscle specimen sets recorded on 600 and 300 MHz spectrometers at different spinning speeds (left). RF inhomogeneity conditions are as summarized by Eq. (9), with $(a_1, a_2, a_3) = (0.025 \pm 0.01, 0.099 \pm 0.005, 0.10 \pm 0.03)$ and $(0.15 \pm 0.01, 0.074 \pm 0.006, 0.072 \pm 0.017)$ for the 600 and 300 MHz experiments, respectively. Simulation details are given in the Appendix.
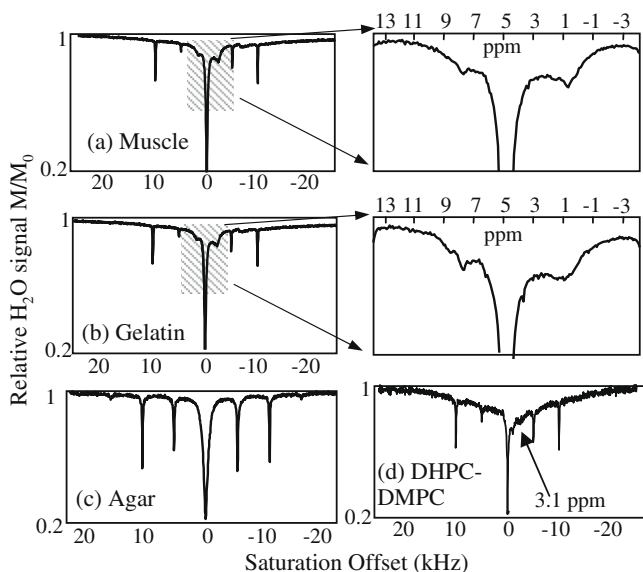
Fig. 6. MTMAS z-spectra measured on a 600 MHz spectrometer at 4 °C and 5 kHz spinning speed for (a) muscle tissue; (b) a 10% Gelatin gel; (c) 6% Agar; (d) a 3:2 DHPC-DMPC suspension. The shaded areas indicated in (a) and (b) are expanded on the right and their scale has been translated into a conventional ppm scale (referenced to H_2O at 4.8 ppm), to highlight their shared isotropic features.

saccharide) or DHPC-DMPC (a model membrane). Since Gelatin contains mainly Glycine and Proline but has less than 2% aromatic amino acids, we assign the main three peaks mentioned above to macromolecular aliphatic (1.2 and 1.8 ppm) and to amide (7.3 ppm) protein protons.

Although the sharpness and non-labile nature of the aliphatic protons leaves cross-relaxation in the slow tumbling regime as the sole mechanism capable of originating MT absorption features at 1.2 and 1.8 ppm, the lability of amide protons opens the possibility of a CEST contribution to the 7.3 ppm absorption. In order to evaluate the possibility of having multiple transfer mechanisms operating simultaneously for this peak we decided to model the MT traces with a set of four Bloch equations, coupled by magnetization exchange terms. These four reservoirs represent the liquid water, the 7.3 ppm amide protons, the 1.2 ppm aliphatics and the 1.8 ppm aliphatics. In order to further constraint these simulations, the ratio between the combined concentrations of the 1.2 and 1.8 ppm aliphatic protein protons and the concentration of amide protein protons was taken to be 6:1; a number fixed as per the un-weighted count of their occurrence in all amino acids under the assumption that the latter are all equally represented in a tissue sample. With the chemical shift and relative concentrations of all sites thus known, and with the H_2O relaxation parameters set as for Fig. 5, remaining values needed to be fit include the absolute protein concentration, the k^{MT}'s and the protein sites T_1 and T_2. Fig. 7 presents a typical best fit of the experimental data for a muscle specimen spinning at 5 kHz, as well as the best-fit numbers arising from extensive simulations of these data. Although a range of parameters could fit equally well these experimental data, an important aspect of these fits concerns the fact that, for a given overall protein concentration and for comparable aliphatic and amide T_1, T_2 values, the rates for aliphatic and amide MT ended up being very similar. Since aliphatic groups do not contain any exchangeable protons this coincidence suggests that the main process originating all these high-resolution MT features is in fact reflecting cross-relaxation, with little or no additional contributions from a CEST-like amide exchange.
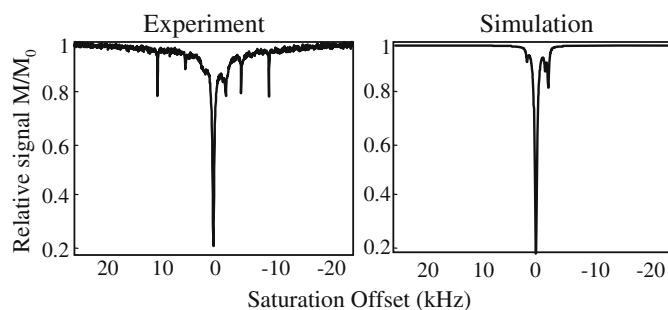

Fig. 7. Comparison between a MTMAS spectrum measured on a muscle tissue at 600 MHz and a 5 kHz spinning speed (left), and a simulation based on exchange coupled Bloch equations possessing four spin pools: a water reservoir (4.8 ppm), two aliphatic (1.2 and 1.8 ppm) protons, and an amide one (7.3 ppm). A priori fixed parameters of these simulations included T_1^{water} = 2800 ms, T_2^{water} = 500 ms, $T_1^{aliphatics}$ = T_1^{amide} = 1000 ms, $T_2^{aliphatics}$ = T_1^{amide} = 50 ms, [^{1}H]$_{water}$ = 100 M, [^{1}H]$_{aliphatics}$/ [^{1}H]$_{amide}$ = 6. Experiments could then be fit equally well over the [^{1}H]$_{aliphatics}$ = 0.78– 0.15 M range, and by corresponding magnetization transfer rates $k_{MT}^{aliphatic\ water}$ = 9– 18 Hz, $k_{MT}^{aliphatic\ water}$ = 12–22 Hz.

3.4. Anisotropic MTMAS features arising at higher spinning rates

All data presented so far was collected at relatively slow MAS rates, which both previous HRMAS studies [5–7,42,43] as well as our own histological tests (vide infra), reveal as acceptable from a tissue integrity point of view. Fig. 8 presents MTMAS spectra of a muscle tissue recorded at different, higher spinning speeds. Upon raising the spinning speed the broad baseline appearing at even moderate MAS rates sharpens further, and begins to evidence a solid-like spinning sideband manifold. This pattern only becomes clear at relatively high (≥10 kHz) MAS rates and, by contrast to what was introduced in Paragraph 3.2, it represents a 'genuine' MTMAS transfer between water and macromolecules. Notably, its field-independent center of mass is positioned at 3.1 ppm; this position is reminiscent of the feature observed in the MTMAS of membrane-like environments, rather than on the protein (Gelatin) sample. As this MAS feature emerges from the broad (≥50 kHz wide) baseline arising in static MT experiments, it gives evidence on the latter's chemical origin. With such new, 'fifth' site resolved, a series of exchange-type simulations of the kind described above were repeated. For simplicity these were still circumscribed to a four-site model, involving this time the isotropic water, an aliphatic protein site, an amide site and this new additional solid-like site (Fig. 9). Best-fit parameters accounting for this new site included T_1 = 1000 ms, T_2 = 83 μs and for a 4 M concentration for this 3.1 ppm peak, a water exchange rate k^{MT} ≈ 33 Hz. This exchange rate is similar to the one extracted for the aliphatic and amide protons, and suggests again that the main mechanism involved in the MT pathway between the water and the narrowed macromolecular protons is cross-relaxation. Unfortunately, as illustrated in Fig. 10, histology also reveals that tissue damage begins to occur at the fast spinning speeds needed to resolve these high-resolution features. Proceeding further with these characterizations and fully exploring the nature of this spectroscopic signature, will therefore require other techniques that circumvent the use of high spinning speeds into this kind of MT experiment.

3.5. MAS: reproducibility and reliability on tissue samples

In order for MAS-based procedures like the one here described to be relevant in biological studies, one needs to determine the fate of the specimens as they undergo different treatments including sample preparation, handling, and spinning inside the spectrometer. To assess the reproducibility of
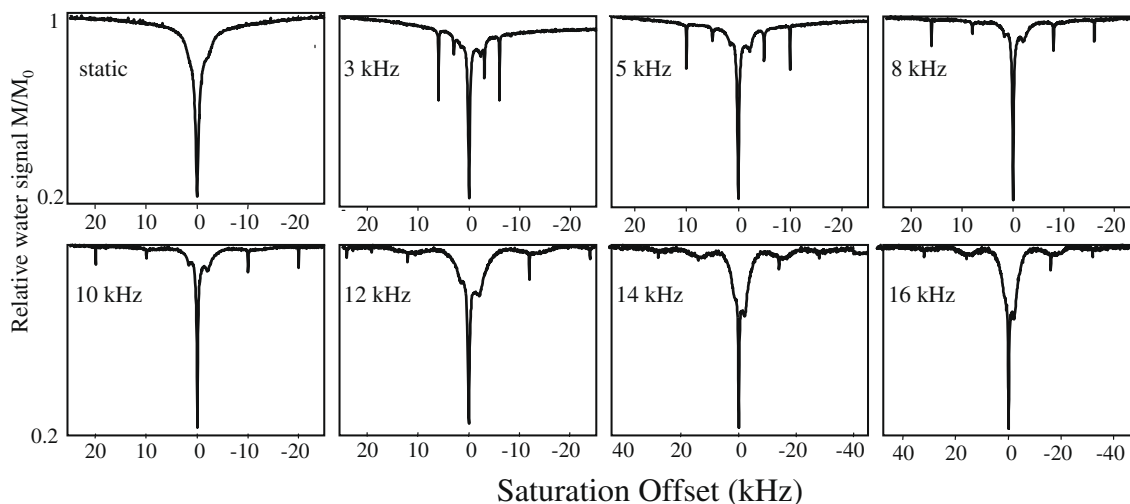
Fig. 8. MTMAS NMR z-spectra measured for a muscle tissue specimen at increasing spinning speeds (600 MHz, 4 °C), revealing the onset of a line-narrowing process of the broad background resonance beyond 10 kHz rates.
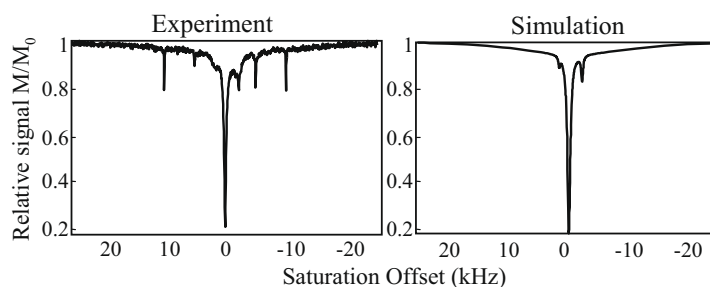

Fig. 9. Idem as in Fig. 7, but this time incorporating a fifth site into the pool of exchanging protons corresponding to a macromolecular baseline centered at 3 ppm.
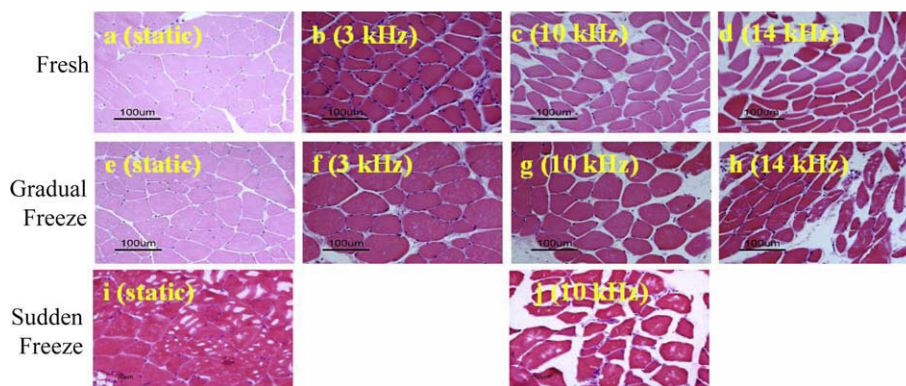

Fig. 10. Paraffin blocks of muscle fibers showing histological cross sections stained with hematoxylin-eosin. (a–d) Fresh, unfrozen samples. (e–h) Samples that were subject to a slow freezing procedure with dry ice. (i and j) Samples that were subject to snap-freezing in liquid nitrogen. (a) Fresh excised control kept at 4 °C. (b) Idem as (a) after 3 kHz spinning for 60 min. (c) Idem for 10 kHz spinning. (d) Idem for 14 kHz. (e) Dry-ice frozen control at 4 °C. (f) Idem after 3 kHz spinning for 60 min. (g) Idem for 10 kHz spinning. (h) Idem for 14 kHz. (i) Sudden liquid -nitrogen frozen control. (j) Idem after 10 kHz spinning for 60 min.

HRMAS in general, and of MTMAS tissue experiments in particular, specimens were subject to a variety of preparation and sample spinning conditions. While all these different samples yielded similar spectral sideband patterns both in their MTMAS their HRMAS traces (not shown), their histological sections were quite different. We observed that specimens subject to a gradual (dry-ice-based) freezing protocol showed only slight compromises in their histological qualities vis-á-vis a static control sample, all the way until reaching spinning speeds of ca. 10 kHz. Damage to the structure of the cells, however, resulted at higher spinning rates, with a concomitant degradation of the tissues' organization (Fig. 10). On the other hand, much more sever changes were observed upon subjecting specimens to snap-shot freezing with liquid nitrogen even in the absence of spinning, probably the result of a formation of extra-cellular microcrystalline ice. Still, it should be pointed out that if keeping temperatures at ≈4 °C during the NMR analyses to suppress degradation processes, fully reversible changes were observed in the HRMAS and MTMAS traces even upon spinning in excess of 16 kHz, regardless of the sample freezing protocol used.

4. Discussion and conclusions

MT experiments carried out under MAS carry a promise to improve the resolution of the water saturation process in tissues, and thereby help reveal hitherto unresolved aspects of this kind of experiments. Indeed upon execution of MTMAS, highly resolved features reminiscent to those associated to the averaging out of second-rank anisotropies arose. Further examinations, however, revealed that the strong sideband patterns observed in MTMAS NMR experiments were also observed upon spinning liquid water at or off the magic axis, suggesting that the origin of these sidebands relates to time-dependent RF inhomogeneities rather than from "structural" waters. Although the appearance of small inhomogeneity-induced sidebands upon the spinning of a sample had been predicted in early liquid-state experiments [49], these effects become amplified by several orders of magnitude when considering saturation transfer experiments. A suitable modeling of the RF field distribution within the solenoid coil could indeed explain this new kind of sideband pattern; although undesired in this case, such off-resonance saturation could conceivably become useful in a controlled setting for a variety of purposes (like the imaging of samples). In addition to these sideband manifolds, MTMAS experiments performed at moderate spinning speeds revealed a net saturation of the water when irradiating at ≈ 1.2, 1.8 and 7.3 ppm. The fact that these features were nearly independent of tissue type suggests that in spite of the latter's complex molecular environment, the nature of these MT exchanging sites are fairly similar. In order to determine which of the tissue components could be responsible for these MT absorptions studies were performed on a protein, a polysaccharide and a model membrane sample. The resolved tissue features were only visible in the MTMAS trace of Gelatin, suggesting that these novel spectral features arise from the protein matrix rather than from polymeric sugars or lipids. Further insight on the actual MT mechanism connecting these sites with the water was sought from a Bloch equation model involving exchange-type terms; the similar MT rates then found for the aliphatic and amide protons—which agree with those determined in rat brain [53] and cartilage [54] studies done by alternative means—suggest that the major mechanism contributing to MT in these experiments (or at least the rate-determining transfer step) comes from cross-relaxation rather than from chemical exchange for all sites. Further confirmation of this observation based on variable-temperature and variable-pH measurements, are planned.

In addition to these newly resolved features, both static and moderate-rate MAS experiments on biological tissues detect a broad, ca. 50 kHz wide MT base. MAS yields little resolution of this broad background until reaching ∼10 kHz spinning rates; at this point a new line-narrowing process becomes evident, this time associated to "legitimate" MT spinning sidebands. Interestingly, the center of mass of this new manifold is shifted from both the liquid H_2O and the protein resonances; its ≈ 3 ppm shift is akin to the main feature arising upon executing MTMAS on a DHPC-DMPC model, suggesting a membrane origin. Tissue integrity issues prevented us from further exploiting this promising feature; we are attempting to further clarify it from ongoing experiments involving MTMAS at slow spinning rates, executed in conjugation with homonuclear line-narrowing pulse sequences [55]. When considered in conjunction to the protein cross-relaxation peaks, these lipid-based exchanges agree with the picture afforded by Singer and coworkers based on NOE measurements [47].

Overall we believe that, if suitably performed and analyzed, the MTMAS technique could assist in clarifying some of the features involved in static MT measurements. Although executed by necessity under ex vivo conditions, this new information could in turn become an important aid to better understand the spin physics and the tissue-water interactions arising in MT experiments carried out in both spectroscopic- and in clinical-oriented setting.

Appendix A

Simulations based on the steady-state solution for the Bloch Equations

The effect of the MAS-modulated RF pulse on the water proton spins was modeled with a single set of Bloch equations:

$$\frac{dM_x}{dt} = \delta\omega \cdot M_y - \gamma B_{1y}(t) \cdot M_z - \frac{M_x}{T_2} \tag{12a}$$

$$\frac{dM_y}{dt} = \gamma B_{1x}(t) \cdot M_z - \delta\omega \cdot M_x - \frac{M_y}{T_2} \tag{12b}$$

$$\frac{dM_z}{dt} = \gamma B_{1y}(t) \cdot M_x - \gamma B_{1x}(t) \cdot M_y - \frac{M_z}{T_1} + \frac{M_0}{T_1} \tag{12c}$$

Since the RF irradiation is time-dependent (Eq. (4)), an approximate numerical simulation was performed by partitioning the RF pulse into many short time intervals dt over which it was assumed that the precession of the magnetization vector and the effects of T_1 and T_2 relaxation were small enough not to influence each other, and that the RF pulse could be considered constant. The simulation was based on two separate analytical solutions to the Bloch equations for a constant RF pulse without relaxation terms (Eq. (13)) and for relaxation included without an RF pulse (Eq. (15)). The two solutions were repeatedly applied over the short time intervals $dt = t_f - t_o$, by first solving for the value of $M(t_f)$ with Eq. (14) for the RF pulse and chemical shift kept constant at the value of $B(t_o)$. The relaxation equations were then solved over the same time interval dt by substituting the $M(t_f)$ obtained from Eq. (16) for $M(t_o)$ in Eq. (14). This approximation is permissible as long as the time step used (0.01 ms) is much smaller than the precession rate of the magnetization vector $2\pi/\delta\omega$, than the relaxation times T_1 and T_2, and than the period of the RF nutation $2\pi/\gamma B_1$. The system was determined to have reached steady state at $t = 5^{*}T_1$.

Constant RF pulse Equations:

$$\frac{dM_x}{dt} = \delta\omega \cdot M_y - \gamma B_{1y} \cdot M_z \tag{13a}$$

$$\frac{dMy}{dt} = \gamma B_{1x} \cdot Mz - \delta\omega \cdot Mx \tag{13b}$$

$$\frac{dM_z}{dt} = \gamma B_{1y} \cdot M_x - \gamma B_{1x} \cdot M_y \tag{13c}$$

Solution:

$$M(t_f) = M(t_o) \cdot e^{iB \cdot dt} \tag{14}$$

where $B = \begin{pmatrix} 0 & \delta\omega & -\gamma B_{1y} \\ -\delta\omega & 0 & \gamma B_{1x} \\ \gamma B_{1y} & -\gamma B_{1x} & 0 \end{pmatrix}$.

Relaxation Equations:

$$\frac{dM_x}{dt} = -\frac{M_x}{T_2} \tag{15a}$$

$$\frac{dM_y}{dt} = -\frac{M_y}{T_2} \tag{15b}$$

$$\frac{dM_z}{dt} = -\frac{M_z}{T_1} + \frac{M_0}{T_1} \tag{15c}$$

Solutions:

$$M_x(t_f) = M_x(t_0)e^{-\frac{dt}{T_2}}$$
$$M_y(t_f) = M_y(t_0)e^{-\frac{dt}{T_2}} \tag{16}$$
$$M_z(t_f) = M_z(t_0)(1 - e^{-\frac{dt}{T_1}})$$

For achieving a best fit of the data Eqs. (9)–(11) were used, with $\gamma B_1^{ax}/2\pi \approx 0.1$ kHz, a Gaussian distribution of offsets over 80 Hz to account for shimming and other heterogeneities, and T_1, T_2 H_2O values of 2800 and 500 ms, respectively. The simulations were performed separately for two different field strengths and MAS probes, operating at 600 and 300 MHz.

References

[1] R.A. de Graaf, In-Vivo NMR Spectroscopy: Principles and Techniques, Wiley, 2007.
[2] P.A. Bottomley, Spatial localization in NMR spectroscopy in vivo, Ann. N. Y. Acad. Sci. 508 (1987).
[3] C. Faber, Ann. Rep. NMR Spectroscopy 61 (2007) 1–50.
[4] S.A. Roll, W. Dreher, E. Busch, D. Leibfrtiz, Magn. Reson. Med. 39 (1998) 742–748.
[5] B. Sitter, U. Sonnewald, M. Spraul, H.E. Fjosne, I. Gribbestad, NMR Biomed. 15 (2002) 327–337.
[6] H. Lyng, B. Sitter, T.F. Bathen, L.R. Jensen, K. Sundfor, G.B. Kristensen, I. Gribbestad, BMC Cancer 7 (2007) 7–11.
[7] L.L. Cheng, I.-W. Chang, B.L. Smith, R.G. Gonzalez, J. Magn. Reson. 135 (1998) 194–202.
[8] S. Forsen, R.A. Hoffman, J. Chem. Phys. 39 (1963) 2892–2901.
[9] S.D. Wolff, R.S. Balaban, Magn. Reson. Med. 10 (1989) 135–144.
[10] J. Grad, R.G. Bryant, J. Magn. Reson. 90 (1990) 1–8.
[11] T.L. Ceckler, S.D. Wolff, S.A. Simon, V. Tip, R.S. Balaban, J. Magn. Reson. 98 (1992) 637–645.
[12] D.K. Kim, T.L. Cekler, V.C. Hascall, A. Calabrs, R.S. Balaban, Magn. Reson. Med. 29 (1993) 211–215.
[13] R.G. Bryant, Annu. Rev. Biophys. Biomol. Struct. 25 (1996) 29–53.
[14] R.M. Henkelman, G.J. Strainsz, S.J. Graham, NMR Biomed. 14 (2001) 57–64.
[15] D. Leibfritz, W. Dreher, NMR Biomed. 14 (2001) 65–76.
[16] U. Eliav, G. Navon, J. Am. Chem. Soc. 124 (2002) 3125–3132.
[17] B.P. Hills, F.A. Fauret, J. Magn. Reson. B103 (1994) 142–151.
[18] E. Liepinsh, G. Otting, Magn. Reson. Med. 35 (1996) 30–42.
[19] D.F. Gochberg, R.D. Kennan, M.J. Marynski, J.C. Gore, J. Magn. Reson. 131 (1998) 191–198.
[20] J. Zhou, P.C.M. van Zijl, Prog. NMR Spectrosc. 48 (2006) 109–136.
[21] S.D. Wolff, R.S. Balaban, Magn. Reson. Med. 86 (1990) 164.
[22] H. Braak, E. Braak, Acta Neuropathol. 82 (1991) 239–259.
[23] H. Hanyy, S. Shimizu, Y. Tanaka, H. Kanetaka, T. Iwamoto, K. Abe, Neurosci. Lett. 380 (2005) 166–169.
[24] M. Bozzali, M. Franceschi, A. Falini, S. Pontesilli, M. Cercignani, G. Magnani, G. Scotti, G. Comi, M. Filippi, Neurology 57 (2001) 1135–1137.
[25] J.R. Peterella, R.I. Grossman, J.C. McGowan, G. Campbell, J.A. Cohen, Am. J. Neuroradiol. 17 (1996) 1041–1049.
[26] N.C. Silver, M. Lai, M.R. Symms, G.J. Barker, W.I. McDonald, D.H. Miller, Neurology 51 (1998) 758–764.
[27] G.E. Santyr, F. Schnideider, J. Magn. Reson. Imag. 1 (1996) 203–212.
[28] S.D. Wolff, S. Chesnick, J.A. Frank, K.O. Lim, R.S. Balaban, Radiology 179 (1991) 623–628.
[29] V. Guivel-Scharen, T. Sinnwell, S.D. Wolff, R.S. Balaban, J. Magn. Reson. 133 (1998) 36–45.
[30] S. Aime, D. Delli Castelli, E. Terreno, J. Am. Chem. Soc. 124 (2002) 9364–9365.
[31] J. Zhou, J. Payen, D.A. Wilson, J. Laterra, P.C.M. van Zijl, Nat. Med 9 (2003) 1085–1090.
[32] S. Aime, D. Delli Castelli, Angew. Chem. Int. Ed. Engl. 41 (2002) 4334–4336.
[33] F.A. Van Dorsten, M. Wyss, T. Wallimann, K. Nicolai, Biochem. J. 325 (1997) 411–416.
[34] K.M. Brindle, M.J. Blackedge, R.A.J. Challiss, G.K. Radda, Biochemistry 28 (1989) 4887–4893.
[35] K.M. Ward, A.H. Aletras, R.S. Balaban, J. Magn. Reson. 143 (2000) 79–87.
[36] S. Aime, S.G. Cricj, E. Gianolio, G.B. Giovenzana, L. Tei, E. Terreno, Coord. Chem. Rev. 250 (2006) 1562–1579.
[37] M. Woods, D.E. Woessner, D. Sherry, Chem. Soc. Rev. 35 (2006) 500–511.
[38] M.J. Duer, Introduction to Solid-State NMR Spectroscopy, Blackwell Science, UK, 2002.
[39] E.R. Andrew, A. Bradbury, R.G. Eades, Nature 183 (1959) 1805–1806.
[40] I.J. Lowe, Phys. Rev. Lett. 2 (1959) 285–289.
[41] J. Herzfeld, A.E. Beger, J. Chem. Phys. 73 (1980) 6021.
[42] P. Weybright, K. Millis, N. Campbell, D.G. Cory, S. Singer, Magn. Reson. Med. 39 (1998) 337–345.
[43] J.-H. Chen, E.B. Sambol, P.T. Kennealy, R.B. O'Connor, P.L. DeCarolis, D.G. Cory, S. Singer, J. Magn. Reson. 171 (2004) 143–150.
[44] L.L. Cheng, M.J. Ma, L. Becerra, T. Hale, I. Tracey, A. Lackner, R.G. Gonzalez, Proc. Natl. Acad. Sci. USA 94 (1997) 6408–6413.
[45] B. Sitter, S. Lundgren, T.F. Bathen, J. Halgunset, H.E. Fjosne, I.S. Gribbestad, NMR Biomed. 19 (2006) 30–40.
[46] S. Garrod, E. Humpfer, S.C. Connor, S. Polley, J. Connelly, J.C. Lindon, J.K. Nicholson, E. Holmes, Magn. Reson. Med. 41 (1999) 1108–1118.
[47] J.-H. Chen, E.B. Sambol, P. DeCarolis, R. O'Connor, R.C. Geha, Y.V. Wu, S. Singer, Magn. Reson. Med. 55 (2006) 1246–1256.
[48] J.F.A. McManus, R.W. Mowary, Staining Methods, Hoeber, 1960.
[49] D.I. Hoult, R.E. Richards, Proc. R. Soc. Lond. A 344 (1975) 311–340.
[50] P. Tekely, M. Goldman, J. Magn. Reson. 148 (2001) 135–141.
[51] K. Elbayed, B. Dillmann, J. Raya, M. Piotto, F. Engelke, J. Magn. Reson. 174 (2005) 2–26.
[52] D.C. Williamson, J. Narvainen, P.L. Hubbard, R.A. Kauppinen, G.A. Morris, J. Magn. Reson. 183 (2006) 203–212.
[53] P.C.M. Van Zijl, J. Zhou, N. Morin, J.F. Payen, D. Wilson, S. Mori, Magn. Reson. Med. 49 (2003) 440–449.
[54] W. Ling, R.R. Regatte, G. Navon, A. Jerschow, Proc. Natl. Acad. Sci. USA 105 (2005) 2266–2270.
[55] P. Caravatti, P. Neuenschwander, R.R. Ernst, Macromolecules 18 (1985) 119–122.